How to cite: *Angew. Chem. Int. Ed.* **2023**, *62*, e202304978
doi.org/10.1002/anie.202304978

Lithium Metal Batteries

Anode-Free Lithium Metal Batteries Based on an Ultrathin and Respirable Interphase Layer

Yan Wang, Zongtao Qu, Shitao Geng, Meng Liao, Lei Ye, Zulipiya Shadike, Xiaoju Zhao, Shuo Wang, Qiuchen Xu, Bin Yuan, Xiao Zhang, Xiaxin Gao, Xuesong Jiang, Huisheng Peng, and Hao Sun**

Abstract: Anode-free lithium (Li) metal batteries are desirable candidates in pursuit of high-energy-density batteries. However, their poor cycling performances originated from the unsatisfactory reversibility of Li plating/stripping remains a grand challenge. Here we show a facile and scalable approach to produce high-performing anode-free Li metal batteries using a bio-inspired and ultrathin (250 nm) interphase layer comprised of triethylamine germanate. The derived tertiary amine and Li_xGe alloy showed enhanced adsorption energy that significantly promoted Li-ion adsorption, nucleation and deposition, contributing to a reversible expansion/shrinkage process upon Li plating/stripping. Impressive Li plating/stripping Coulombic efficiencies (CEs) of ≈99.3 % were achieved for 250 cycles in Li/Cu cells. In addition, the anode-free $LiFePO_4$ full batteries demonstrated maximal energy and power densities of 527 Wh kg^{-1} and 1554 W kg^{-1}, respectively, and remarkable cycling stability (over 250 cycles with an average CE of 99.4 %) at a practical areal capacity of ≈3 mAh cm^{-2}, the highest among state-of-the-art anode-free $LiFePO_4$ batteries. Our ultrathin and respirable interphase layer presents a promising way to fully unlock large-scale production of anode-free batteries.

Introduction

The ever-growing demands on prolonged endurance of consumer electronics and electric vehicles have driven the pursuit of high-energy-density Li-ion batteries.[1–5] Li metal was widely recognized as the 'Holy Grail' anode owing to the high theoretical specific capacity (3860 mAh g^{-1}) and low redox potential (−3.04 V vs. standard hydrogen electrode).[6–10] The use of highly excessive Li metal, however, leads to severe safety and processing complexity that hinders the practical applications of lithium metal batteries (LMBs).[11–13] Therefore, anode-free batteries without the use of any lithium metal during battery production are desirable alternatives with overwhelming advantages in energy density, cost and production convenience.[14–16] However, the poor CE and cycling stability have severely hindered their mass applications.[17,18] Considerable efforts have been made on electrolyte composition,[19–22] anode/electrolyte interface,[23–25] cathode sacrificial agent[15] and cycling condition (pressure and depth of discharge).[26,27] However, realizing both high CE and cycling stability remains a long-standing challenge for the whole field, owing to uneven Li deposition and severe parasitic reaction between Li deposition and electrolyte.

Engineering anode/electrolyte interface represents a promising approach towards high-performing anode-free LMBs.[23,28] The interphase layer serves as an effective physical barrier that suppresses the continuous side reactions between Li deposition and electrolyte, and participates in solid-electrolyte interphase (SEI) formation.[29–35] However, these thick (1–10 μm) interphase layers inevitably sacrifice the energy density of anode-free batteries.[28,32] In addition, they cannot afford highly reversible Li plating/stripping processes owing to the week interaction with Li metal, resulting in poor cycling performances.[36,37] Therefore, developing ultrathin (e.g., submicrometer) and strongly interacted interphase layer for anode-free LMBs with high

[*] Dr. Y. Wang, Z. Qu, S. Geng, Dr. X. Zhao, S. Wang, Q. Xu, B. Yuan, Dr. X. Zhang, X. Gao, Prof. X. Jiang, Prof. H. Sun
Frontiers Science Center for Transformative Molecules, School of Chemistry and Chemical Engineering, and Zhangjiang Institute for Advanced Study, Shanghai Jiao Tong University
200240 Shanghai (China)
E-mail: haosun@sjtu.edu.cn

Dr. M. Liao, Dr. L. Ye, Prof. H. Peng
State Key Laboratory of Molecular Engineering of Polymers, Department of Macromolecular Science, and Laboratory of Advanced Materials, Fudan University
200438 Shanghai (China)
E-mail: penghs@fudan.edu.cn

Prof. Z. Shadike
Institute of Fuel Cells, Interdisciplinary Research Center, School of Mechanical Engineering, Shanghai Jiao Tong University
200240 Shanghai (China)

CEs (>99 %) and practical areal capacities (≈3 mAh cm^{-2}) presents a grand challenge for the whole field.

Here we show high-performing anode-free LMBs based on an ultrathin (≈250 nm) and ultralight (≈0.05 mg cm^{-2}) interphase layer. The interphase layer comprised of triethylamine germanate (TEG) can be incorporated on Cu foil through a facile and scalable method, and reversibly expands/shrinks mimicking the human lung to accommodate the volume change during Li plating/stripping. Mechanism studies show the synergistic effect of triethylamine and germanate facilitates Li-ion absorption and nucleation into a dense and uniform deposition layer and induces the formation of lithium fluoride (LiF) and lithium nitride (Li_3N)-rich passivation layer on Li deposition, which significantly promotes Li plating/stripping reversibility. In Li/Cu half cells, they delivered a high average CE of ≈99.3 % for 250 cycles at 1 mA cm^{-2} and 1 mAh cm^{-2} and afforded reversible Li plating/stripping at 5 mA cm^{-2} and 2 mAh cm^{-2} for 150 cycles. With a practical areal capacity of ≈3 mAh cm^{-2}, the anode-free $LiFePO_4$ full battery demonstrated maximal energy and power densities of 527 Wh kg^{-1} and 1554 W kg^{-1}, respectively, and showed an impressive cycling stability (250 cycles) with an average CE of 99.4 %, outperforming state-of-the-art $LiFePO_4$ anode-free batteries. The interphase layer engineering presents a promising strategy for immediate scale-up production of practical anode-free batteries and can inspire other battery chemistries towards high energy density and long cycling stability.

Results and Discussion

In our attempts to design artificial layers for anode-free LMBs, we realize that the alveolus and its outside membrane of the human lung represents an inspirable model of efficient mass transfer and morphology control (Figure 1a). During inhalation, the air was subjected to the expanded alveolus with increasing sites for sufficient O_2/CO_2 exchanging, and the thin membrane outside the alveolus further facilitated the gas transfer and restricts the penetration of tissue fluid (Figure 1a).[38] This inspired us to design an ultrathin interphase layer on Cu to promote Li-ion transfer and deposition for anode-free LMBs. In specific, we selected triethylamine germanate as the key building block of the interphase layer, in which the triethylamine cations can enhance the lithiophilic capability and passivate the anode/electrolyte interface, and the germanate anions were expected to generate Li–Ge alloy that served as efficient nucleation sites for compact and uniform Li deposition (Figure 1b). The TEG was synthesized via a one-step reaction between triethylamine (TEA) and germanium dioxide (GeO_2) as follows:

$$GeO_2 + C_6H_{15}N + H_2O \rightarrow C_6H_{15}NH^+HGeO_3^- \quad (1)$$

The existence of –NH and $HGeO_3$ was verified by Fourier transform infrared spectroscopy (FTIR, Figure S1a). The TEG interphase layer was uniformly incorporated onto a meter-scale.

Cu foil via a simple and scalable blade-coating method and showed a thickness of 250 nm with a flat and smooth surface (Figure 1c and Figure S1b). The ultralow areal density (less than 0.05 mg cm^{-2}) also indicated a negligible influence on the energy density of the resulted batteries via TEG incorporation.

For analysis of the detailed chemical composition of our TEG layer, we performed time-of-flight secondary ion mass spectrometry (TOF-SIMS) and X-ray photoelectron spectroscopy (XPS). The formation of $C_6H_{16}NHGeO_3$ was confirmed by the probed $C_6H_{16}NHGeO_3^+$ signal in TOF-SIMS, as well as the pronounced $C_6H_{16}NHGeO_2^+$, $C_6H_{16}NHGe^+$, $C_6H_{16}N^+$ and GeO^+ signals as the dissociated fragments of $C_6H_{16}NHGeO_3$ (Figure 1d). Surface XPS profile also indicated the presence of C, Ge, O, and N elements in the TEG layer, and the N 1s and Ge 3d peaks at 401.2 eV and 33.1 eV could be assigned to C–N and Ge–O groups, respectively, corresponding to the featured components in $C_6H_{16}NHGeO_3$ (Figure 1e and Figure S2a). Besides, the incorporation of TEG layer resulted in significantly decreased intensity of the Cu 2p signal, suggesting that the Cu foil was uniformly covered by the TEG layer (Figure S2b).

We found the TEG significantly improved the electrochemical performances of Li/Cu cells (Figure 2). In fact, A common ether-based electrolyte was used with optimized 1,3-dioxolane/1,2-dimethoxyethane (DOL/DME) ratio and lithium nitrate ($LiNO_3$) content (see details in the Supporting Information and Figure S3a–b). The lower contact angle of the electrolyte on TEG-Cu implied the enhanced electrolyte wettability attributed to TEG (Figure S4a–b). With TEG incorporation, an apparent lithiation plateau started at ≈80 mV during the initial Li deposition at 1 mA cm^{-2} (Figure 2a), which was in accordance with the reduction peaks in the cyclic voltammetry curves (Figure S4c–d), corresponding to the Li–Ge alloying reaction. Owing to the alloying-induced nucleation, the TEG offered a much lower nucleation overpotential (9 mV) compared with bare Cu (20 mV), indicating significantly reduced nucleation energy barrier via TEG incorporation. Moreover, TEG afforded well-retained overpotentials from 5 to 20 mV with increasing current densities from 0.5 to 5 mA cm^{-2}, compared with the sharp overpotential increase from 15 to 91 mV based on bare Cu (Figure 2b). The enhanced nucleation kinetics derived from the TEG layer suggested more uniform nucleation and lithiophilic nature of the Li–Ge alloy and triethylamine matrix.

Achieving high CEs in Li/Cu cells has important implications for cycling stability improvement of anode-free LMBs. TEG contributed to well-overlapped Li plating/stripping profiles for 200 cycles (Figure 2c), outperforming the cycling stability of bare Cu (Figure S5). In addition, our TEG-Cu exhibited a higher initial CE (92.7 %) compared with bare Cu (91.3 %) and could maintain high CEs of ≈99.3 % for over 250 cycles at 1 mA cm^{-2} and 1 mAh cm^{-2}, while bare Li/Cu cell showed drastically decreased CEs after only ≈100 cycles (Figure 2d and Figure S6). We varied the TEG thickness from 125 to 500 nm for electrochemical performance evaluation, and an optimal thickness of 250 nm had been found for the best cycling performance (Fig-

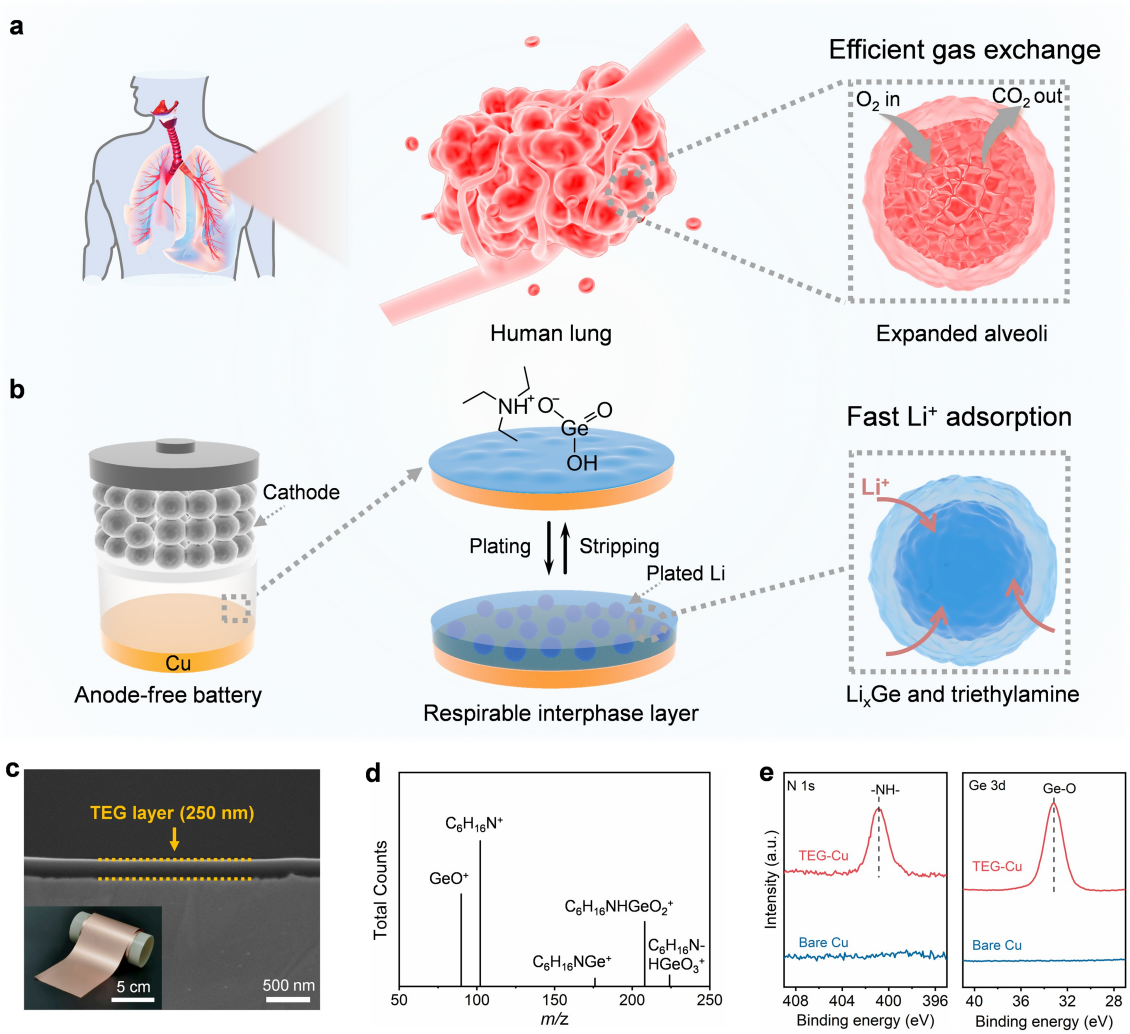

Figure 1. (a) Schematic illustration of the expansion/shrinkage of the alveoli in a human lung during breathing with efficient gas exchange. The magnified image shows the gas exchange process of a single alveolus during inhalation. (b) Schematic illustration of the anode-free battery based on a TEG-modified Cu current collector. The bioinspired TEG layer can reversibly expand/shrink during the Li metal plating/stripping process that suppresses severe volume change and parasitic reactions. The magnified image shows enhanced Li-ion absorption of Li_xGe alloy and triethylamine in TEG. (c) Cross-sectional SEM image of the TEG-Cu current collector. The inset shows a large-area TEG-Cu current collector through a scalable blade-coating process. (d) TOF-SIMS spectrum of the TEG. (e) High-resolution XPS spectra of the N 1s and Ge 3d for bare Cu and TEG-Cu.

ure S7). Even at higher current densities and areal capacities (2 mA cm^{-2}/2 mAh cm^{-2} and 5 mA cm^{-2}/2 mAh cm^{-2}), the TEG afforded superior CEs (98.5 %) and cycling stability (up to 200 cycles) compared with bare Cu (Figure 2e, f and Figure S8a–b). Under harsher conditions, e.g., 5 mA cm^{-2} and 5 mAh cm^{-2}, an average CE of 98.4 % could be retained by TEG after 40 cycles, compared with only two reversible cycles using bare Cu (Figure S8c–d). When pairing with a commercial carbonate electrolyte comprised of 1 M $LiPF_6$ in ethylene carbonate/dimethyl carbonate (EC/DMC, 1:1 in volume), our Li/TEG-Cu cell showed much a higher CE of ≈98 % after 150 cycles compared with only ≈62 % after 50 cycles in Li/Cu cells (Figure S9). Besides, our TEG layers exhibited significantly promoted CEs and cycling performances when incorporated with a nickel foil substrate (Figure S10). These results suggest that the ultrathin TEG layer significantly promotes the kinetics and reversibility of the Li plating/stripping process, especially at high current densities and areal capacities towards practical applications. We further performed Aurbach test to evaluate the Li plating/stripping reversibility using TEG (see details in Supporting Information), and achieved an impressive average CE of 99.31 % (Figure 2g)[23,39] which is highly competitive to the state-of-the-art Li/Cu cells (Figure S11).[40–45] In comparison, bare Cu showed a much lower average CE of 97.84 % with severe polarization (Figure 2g). Nyquist plots exhibited a lower ion transfer resistance using TEG after the first cycle, suggesting the facilitated ion-transfer kinetics (Figure 2h). Furthermore, the ohmic and charge transfer resistances using bare Cu were increased by 64.2 % and 60.8 % after 50 cycles, respectively, indicating continuous electrolyte consumption and propagated SEI formation (Table S1).[46] In sharp contrast, less than 13 % of the resistance increases was demonstrated for TEG, indicating that the ultrathin

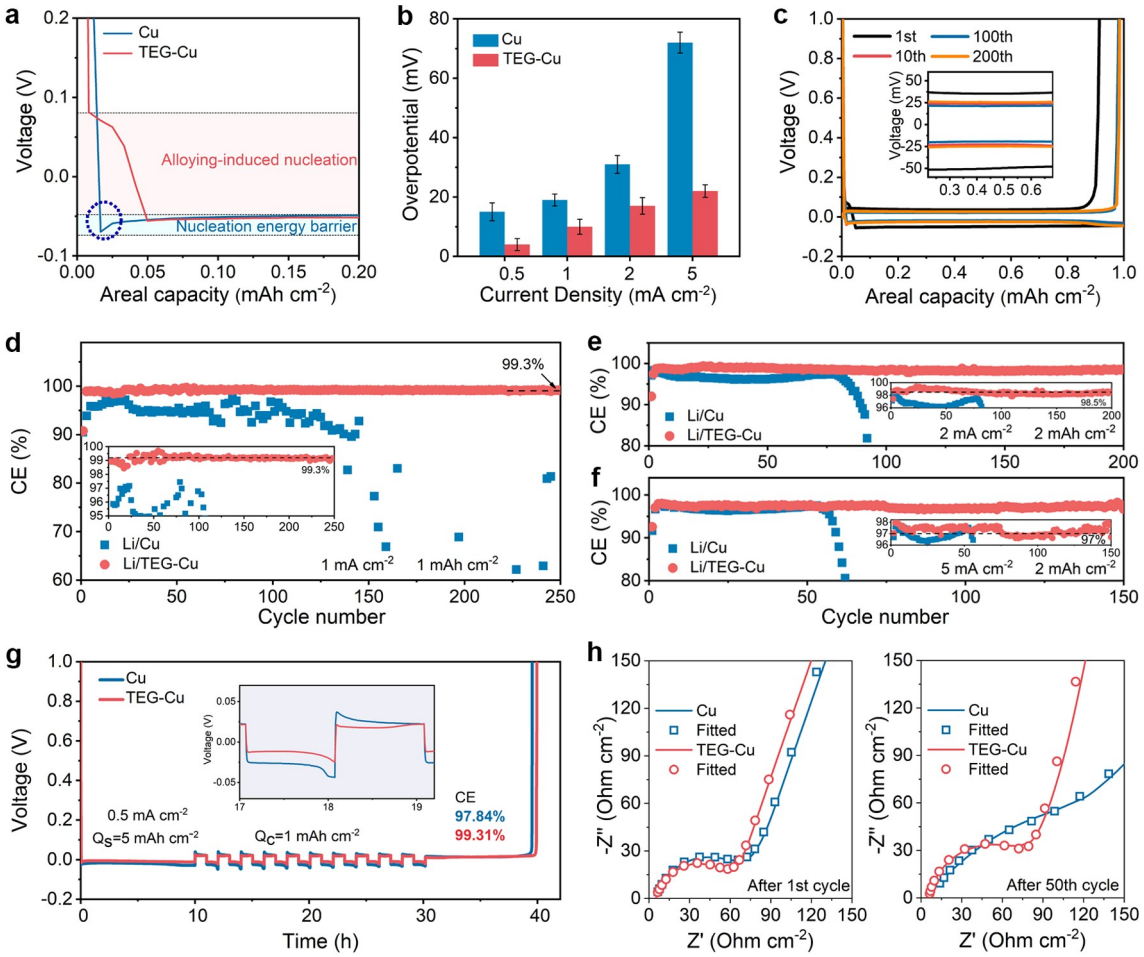

Figure 2. (a) Voltage profiles of the initial Li deposition on bare Cu and TEG-Cu at a current density of 1 mA cm^{-2}. (b) Variation of the Li plating/stripping overpotential on various current densities using bare Cu and TEG-Cu current collectors. (c) Galvanostatic charge–discharge curves of Li/TEG-Cu cells cycled at 1 mA cm^{-2} and 1 mAh cm^{-2}. The inset shows the detailed variation of overpotentials in Li/TEG-Cu cells. (d–f) Coulombic efficiencies (CEs) of Li plating/stripping in Li/Cu cells using bare Cu and TEG-Cu current collectors at the current density and areal capacity of 1 mA cm^{-2} and 1 mAh cm^{-2} (d), 2 mA cm^{-2} and 2 mAh cm^{-2} (e), and 5 mA cm^{-2} and 2 mAh cm^{-2} (f). The insets show the detailed CE variations. (g) Aurbach CE profiles of Li/Cu and Li/TEG-Cu cells at 0.5 mA cm^{-2}. The inset shows the plating and stripping curves, in which Li/TEG-Cu cell exhibits a lower overpotential. (h) Nyquist plots of Li/Cu and Li/TEG-Cu cells after 1st and 50th cycles. Electrolyte for all tests was 1 M LiTFSI in DOL/DME (volume ratio 8/2) with 3 wt% $LiNO_3$.

TEG layer effectively suppressed the unfavored parasitic reactions between the Li deposition and electrolyte, thus affording a highly reversible Li plating/stripping process (Figure 2h). To exclude the influence of the Li counter electrode on the measurement results in two-electrode arrangement,[47] we also prepared Li/Li symmetrical cells under the same condition with Li/Cu cells, which could stably work for 600 cycles without overpotential fluctuation (Figure S12).

The Li deposition morphology shows important effects on the cycling performance of the obtained batteries. With TEG incorporation, the Li deposition on Cu at an areal capacity of 1 mAh cm^{-2} was dense and uniform with a thickness of ≈8 μm (Figure 3a). At higher areal capacities, e.g., 2 mAh cm^{-2} and 5 mAh cm^{-2}, the Li deposition with TEG were dense and uniform with thicknesses of 15 and 40 μm, respectively (Figure 3b–c and S13). In comparison, the much thicker Li deposition suggested the formation of mossy or 'dead' Li on bare Cu at increasing current densities and areal capacities (Figure S14). More importantly, the TEG interphase layer reversibly shrank to ≈330 nm after Li stripping, indicating the reversible expansion/shrinkage process of the TEG layer that accommodates the huge volume change during repeated Li plating/stripping (Figure 3a). In addition, the TEG-Cu layer well maintained the thickness and morphology after Li plating/stripping for 50 cycles (Figure S15). Laser confocal scanning microscopy (LCSM) images further indicated that the Li deposition regulated by TEG was more uniform in height compared with that on bare Cu after 20 cycles (Figure 3d). Atomic force microscopy (AFM) showed that the interphase layer derived from TEG exhibited a much higher average Young's modulus (≈9 GPa) compared with only 2–3 GPa based on bare Cu (Figure 3e), suggesting that TEG contributed to a more robust interphase layer that could accommodate the

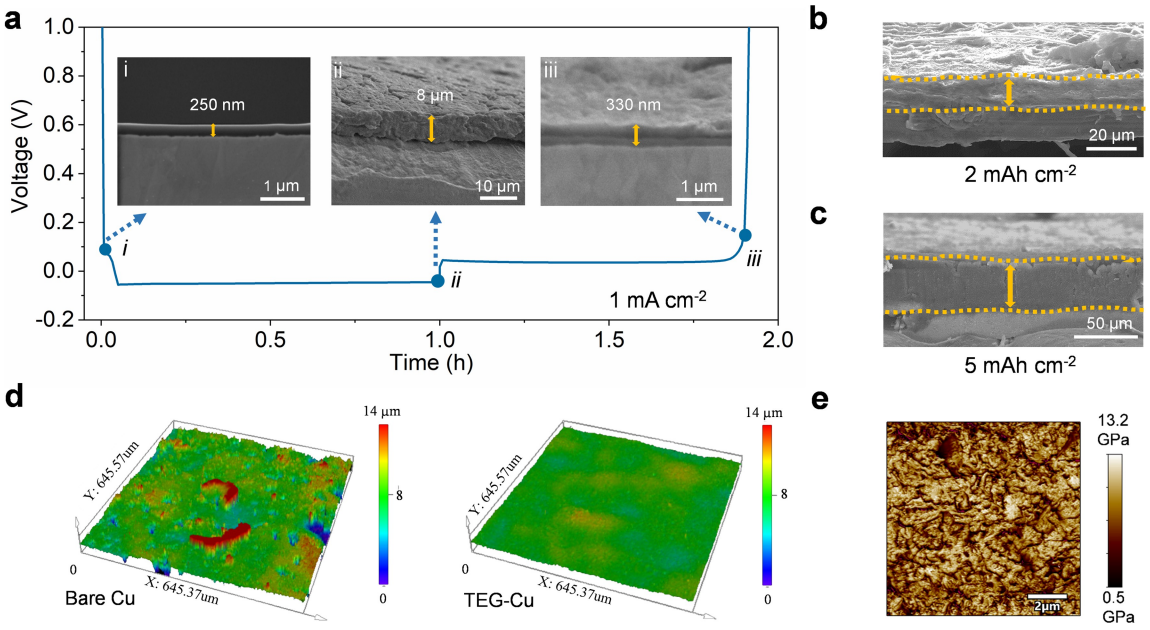

Figure 3. (a) Cross-sectional SEM images of the TEG-Cu current collector at three representative Li plating/stripping states, i.e., as-prepared, after Li plating and after Li stripping. Li plating and stripping were performed at 1 mA cm^{-2} and 1 mAh cm^{-2}. (b–c) Cross-sectional SEM images of the Li deposition on a TEG-Cu current collector with areal capacities of 2 and 5 mAh cm^{-2}, respectively. Li plating and stripping were performed in Li/TEG-Cu cells at 1 mA cm^{-2} for 10 cycles and stopped at the fully plating state for characterization. (d) Three-dimensional distribution of Li deposition on bare Cu (left) and TEG-Cu (right) after 10 cycles constructed from laser confocal scanning microscopy images. The analysis area is 645 × 645 μm^2. Current density and areal capacity, 1 mA cm^{-2} and 1 mAh cm^{-2}, respectively. (e) Young's modulus distribution profile based on atomic force microscopy using TEG-Cu after 10 cycles and stopped at fully stripped state. Current density and areal capacity, 1 mA cm^{-2} and 1 mAh cm^{-2}, respectively.

huge volume change during repeated Li plating and stripping cycles (Figure S16).

The reversible volume change of the TEG layer might originate from the Li_xGe alloy and triethylamine matrix during Li plating and stripping (Figure S17). During the initial Li plating, the lithiation of germanate resulted in the formation of Li_2O and Li_xGe alloy based on the following reactions:[48]

$$GeO_3^- + 6Li^+ \rightarrow Ge + 3Li_2O \quad (2)$$

$$Ge + xLi^+ + xe^- \leftrightarrow Li_xGe \quad (3)$$

The formation of the Li_xGe alloy during the initial Li plating process was verified by the roughened morphology (Figure S18), as well as the pronounced $Li_{15}Ge_4$ signal in X-ray diffraction (XRD) (Figure S19). The subsequent Li plating and stripping process further confirmed the reservation of Li–Ge alloy during Li plating and stripping, e.g., after 10 plating/stripping cycles and stopped at fully stripped state (Figure S19). Density functional theory (DFT) calculation showed that, the Li_xGe alloy and C–N species enhanced the interaction with Li metal ($Li_{15}Ge_4$ of −2.5 eV, C–N of −2.05 eV and Ge–O of −1.25 eV) compared with −1.05 eV of bare Cu (Figure 4a–c and S20), together forming a lithiophilic framework that induced uniform Li deposition and effectively suppressed dendric Li metal formation.[49] During Li stripping, the deposited Li metal was first stripped from the lithiophilic framework, and then de-alloyed from Li_xGe particles, corresponding to the shrinkage of the interphase layer (Figure S17a). The repeated Li plating/stripping process resulted in reversible expansion/shrinkage of the TEG/Li composite layer with significantly promoted CE and cycling stability. In contrast, Li deposition on bare Cu foil was porous and dendric (Figure S14 and S17b), owing to the well-documented lithiophobic nature and sluggish ion-transfer kinetics.[50] The improved nucleation kinetics of Li deposition could be verified by the reduced overpotentials during cycling in Li/TEG-Cu cells (Figure 2c and S5). Therefore, we supposed that the facilitated nucleation kinetics and effective regulation of Li deposition could be maintained for TEG-Cu after cycling.

We used TOF-SIMS to probe the composition and distribution of Li deposition with TEG. The detected signals of C–N, LiGe and Li ions originated from triethylamine cation, Li_xGe alloy and deposited Li metal (Figure S21a). Three-dimensional depth profile further showed the uniform distribution of C–N species on the outer surface (Figure 4d), which could efficiently suppress the parasitic reaction between Li deposition and electrolyte and induce dense Li deposition through enhanced interaction according to DFT calculation (Figure 4a–c). The Li_xGe alloys were uniformly distributed within the Li deposition, providing strongly coupled nucleation sites for dense and uniform Li deposition (Figure 4d).

Understanding the formation mechanism of SEI has important implications for better battery performances.[51]

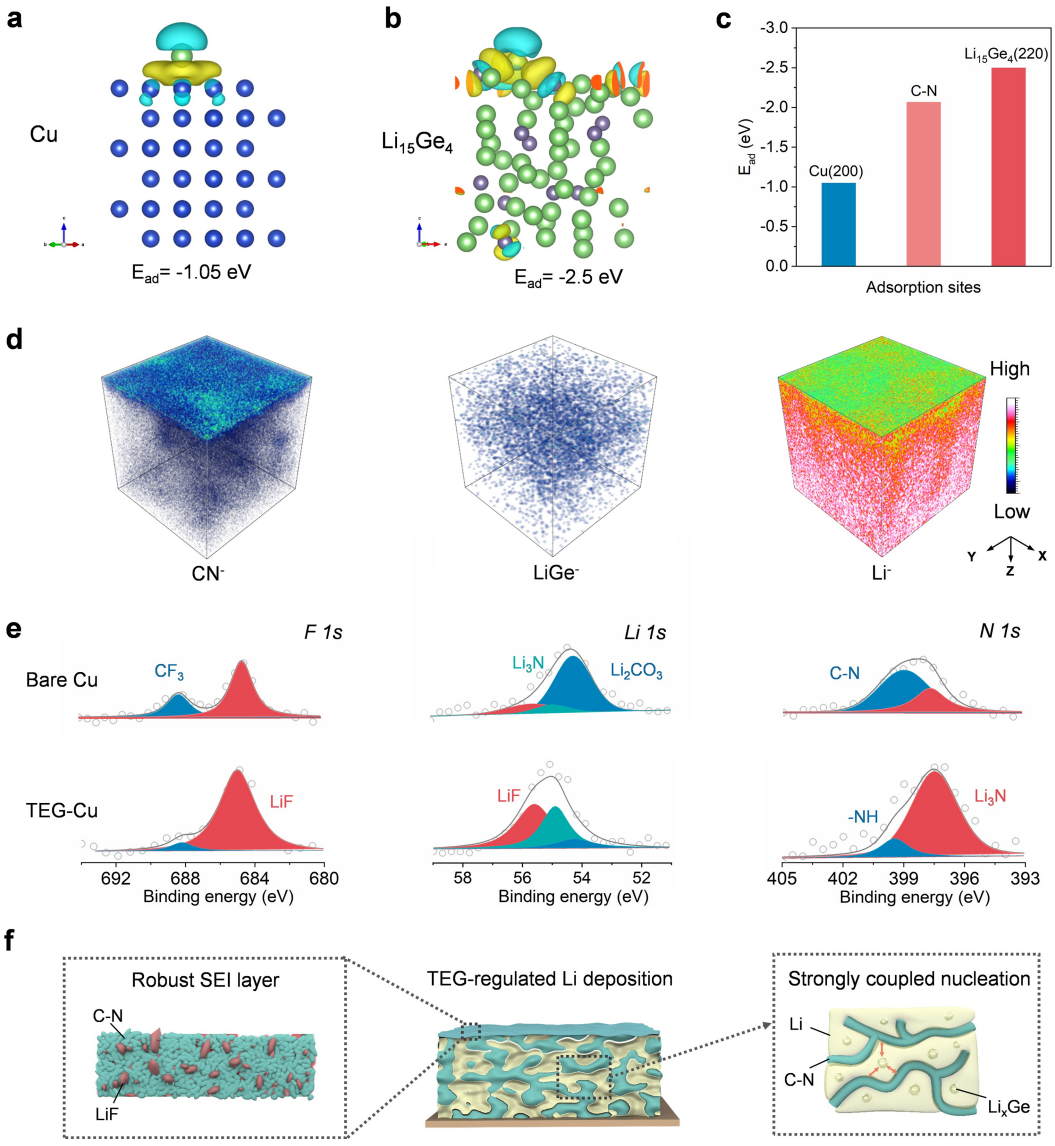

Figure 4. (a–b) Optimized structures and charge density difference plots of Li atom adsorption on Cu and $Li_{15}Ge_4$, respectively. (c) Adsorption energy (E_{ad}) of Li among Cu, C–N and $Li_{15}Ge_4$. (d) Three-dimensional distribution of CN^-, $LiGe^-$ and Li^- constructed based on TOF-SIMS depth scan of the TEG-Cu after Li plating at 1 mA cm^{-2} and 1 mAh cm^{-2}. The analysis area is 50×50 μm^2. (e) High-resolution XPS spectra for F 1s, Li 1s and N 1s of the Li deposition on bare Cu and TEG-Cu after 20 cycles. Current density and areal capacity, 1 mA cm^{-2} and 1 mAh cm^{-2}, respectively. (f) Schematic illustration of the Li deposition on TEG-Cu during repeated plating/stripping processes.

The F 1s and Li 1s spectra of the XPS profile from Li-plated TEG-Cu indicated the formation of a LiF-rich SEI, which might be originated from the facilitated decomposition of $TFSI^-$ into LiF induced by the strong electrostatic interaction between $TFSI^-$ in electrolyte and $–NH^+$ groups in TEG (Figure 4e and S21b), thus facilitating LiF formation.[6,52] In contrast, the Li deposition on bare Cu showed a lower LiF content but higher Li_2CO_3 content that is widely recognized to be insufficient for Li ion transfer and Li metal passivation.[53] Besides, stronger Li_2O and Li_3N signals of TEG-Cu suggested that the TEG participated in SEI formation (Figure S22). Notably, the LiF and Li_3N with low diffusion barrier and high interfacial energy have been proved to effectively promote the flux, nucleation and deposition of Li ions,[39,54] which is consistent with the reduced overpotential values in our Li/TEG-Cu cells. At a higher depth of 20 nm, the intensities of Li_3N and Li_2CO_3 obviously decreased, while the LiF and C–N signals still existed (Figure S23). Therefore, our TEG layer contributed to a lithiophilic framework with promoted Li-ion diffusion and nucleation, as well as a robust SEI that suppressed the parasitic reactions at anode/electrolyte interface, thus achieving significantly improved rate and cycling performances (Figure 4f).

We paired our TEG-Cu current collector with high-mass-loading $LiFePO_4$ (LFP) cathodes for anode-free batteries. At a practical areal capacity of ≈3 mAh cm^{-2} (≈16.9 mg cm^{-2} LFP). The anode-free TEG-Cu/LFP battery

showed much lower overpotentials compared with Cu/LFP battery, e.g., 267 mV vs. 464 mV at 2 C (Figure 5a). Importantly, the TEG contributed to remarkable rate capability of the anode-free batteries, maintaining 84.9 % of the specific capacity with increasing rates from 0.1 to 3 C, compared with only 43.1 % of the capacity retention at 3 C using bare Cu, confirming the promoted kinetics of the Li-ion diffusion and nucleation induced by the TEG layer (Figure 5b and S24). The pursuit of even higher rates depended on the optimization of Li-ion diffusion in the electrolyte according to the diffusion-limited C-rate (DLC) principle.[55] TOF-SIMS verified the formation of an interphase layer comprised of organic C–N and inorganic LiF species on the surface of the Li deposition (Figure S25). In addition, organic C–N species and Li–Ge alloys were uniformly distributed within the Li deposition layer, confirming that the lithiophilic framework could be stably maintained even at 3 mAh cm^{-2}. The corresponding morphology induced by TEG was also verified via SEM and LCSM, which showed more uniform Li deposition on TEG-Cu compared with mossy Li deposition on bare Cu (Figure S26 and S27).

Ragone plot highlighted the advantages of our anode-free batteries in energy and power densities (up to 527 Wh kg^{-1} and 1554 W kg^{-1}, respectively, based on the total mass of active materials on both cathode and anode) compared with state-of-the-art LMBs based on LFP[45,56] and other high-energy-density cathodes such as $LiCoO_2$[13] and $LiNi_{0.5}Mn_{0.3}Co_{0.2}O_2$ (NMC532, Figure 5c).[57] With the use of ultrathin current collector/separator and low-density electrolyte, the energy and power densities of our anode-free

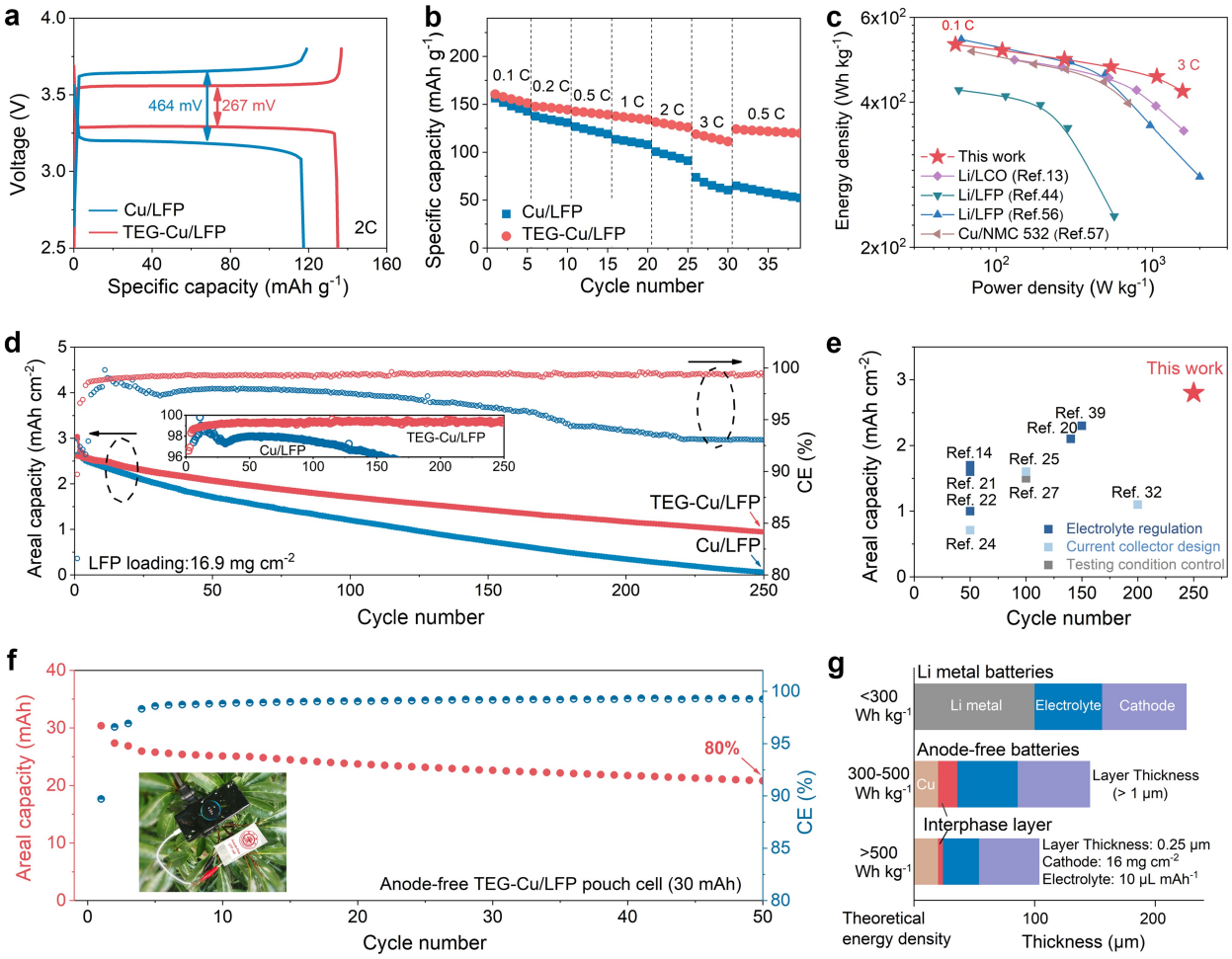

Figure 5. (a) Galvanostatic charge–discharge curves of the anode-free Cu/LFP and TEG-Cu/LFP batteries at a current density of 2 C. (b) Rate performances of anode-free Cu/LFP and TEG-Cu/LFP batteries cycling at increasing rates from 0.1 to 3 C. (c) Ragone plot of our TEG-Cu/LFP full batteries compared with other anode-free and lithium metal full batteries using various cathodes, e.g., $LiFePO_4$,[44,56] $LiCoO_2$[13] and $LiNi_{0.5}Mn_{0.3}Co_{0.2}O_2$ (NMC532).[57] The energy and power densities are calculated from the total mass of the active materials in cathode and anode. (d) Cycling performances of anode-free Cu/LFP and TEG-Cu/LFP batteries with the LFP mass loading of ≈16.9 mg cm^{-2}. The inset shows the detailed CE fluctuations of the TEG-Cu/LFP batteries. (e) The comparison of the areal capacity and cycle number of our TEG-Cu/LFP with state-of-the-art anode-free LFP batteries. (f) Cycling performance of a 30 mAh anode-free TEG-Cu/LFP pouch cell at 0.3 C charge/0.5 C discharge rates. The inset shows our anode-free pouch cell charging a mobile phone. (g) Comparison of the thickness and energy density of conventional Li metal batteries and anode-free Li metal batteries based on thick and ultrathin interphase layers.

batteries can be further promoted at the cell level.[58] More efforts are still underway for further improvement.

Our anode-free batteries also exhibited remarkable cycling stability during 250 cycles with an average CE of 99.4 % (Figure 5d and Figure S28). In-depth analysis of the charge/discharge curves showed that the CEs of the Cu/LFP cell sharply decreased to 97 %–98 % after the initial 10 cycles that was in accordance with the CEs in Li/Cu half cells, which resulted in a more rapid capacity decay of the anode-free Cu/LFP cell. After 170th cycle, the CEs of Cu/LFP further decreased to ≈93 % with significantly increased overpotentials (Figure S29), indicating the significantly increased inner resistance originated from the severe parasitic reaction without TEG. Our anode-free battery represents the highest cycling performance and areal capacity among state-of-the-art anode-free LFP batteries (Figure 5e and Table S2). The theoretical capacity retention in full cells was estimated as 47.1 % based on the CE and initial CE,[18] which was slightly lower than the experimental results (Figure S30). This could be attributed to the Li compensation from lithium salts and additive in electrolyte, as well as the quasi-reversible SEI (such as Li_2O) that prolonged the cycle performance.[18,59] Under lean-electrolyte condition, i.e., a low electrolyte-to-capacity ratio of 10 μL mAh^{-1}, our TEG-based anode-free battery showed a capacity retention of ≈50 % after 150 cycles with an average CE of 99.1 %, compared with only 10 % retention and 97.1 % CE for bare Cu (Figure S31).

We demonstrated the scale-up potential of our anode-free batteries in pouch cells. A 30 mAh TEG-Cu/LFP pouch cell could stably work for over 50 cycles with a capacity retention of ≈80 % and an average CE of more than 99.1 % (Figure 5f). As a proof-of-concept, the anode-free pouch cell could reliably charge a mobile phone and light up 37 commercial LED lamps (Figure 5f and S32). It is worth noting that the use of an ultrathin interphase layer significantly reduces the total thickness of the obtained batteries, which makes our anode-free batteries highly competitive in both volumetric and gravimetric energy densities (Figure 5g and Table S3). In addition, our TEG layer could be used in a variety of other battery systems, such as the highly promising solid-state batteries with the anode-free configuration, which could further promote their safety, energy density, and practicability.[60,61]

Conclusion

In conclusion, we show an ultrathin (250 nm) interphase layer can enable high-performing anode-free LMBs. The triethylamine germanate interphase layer shows enhanced Li adsorption that facilitates Li-ion diffusion, nucleation and deposition, inducing a smooth and dense Li deposition layer with remarkable reversibility. An impressive Li plating/stripping CE of ≈99.3 % is achieved for 250 cycles in Li/Cu cells, and the anode-free $LiFePO_4$ full batteries deliver maximal energy and power densities of 527 Wh kg^{-1} and 1554 W kg^{-1}, respectively, along with excellent cycling stability of 250 cycles. We believe our results can unlock the designing and screening of novel interphase materials towards practical anode-free Li metal batteries and inspire other anode-free battery chemistries such as Na, K and Ca with grand challenges in interface stabilization.

Acknowledgements

This work was supported by NSFC (52122310, 22075050, 22175042, 22209108), STCSM (20JC1414902, 21511104900, 19QA1400800), SHMEC (2017-01-07-00-07-E00062), CPSF (22Z020702143).

Conflict of Interest

The authors declare no conflict of interest.

Data Availability Statement

The data that support the findings of this study are available from the corresponding author upon reasonable request.

Keywords: Anode-Free Battery · Charge Transfer · High Reversibility · Interfaces · Ultrathin Interphase Layer

[1] H. K. Bruce Dunn, J.-M. Tarascon, *Science* **2011**, *334*, 928–935.
[2] J. He, C. Lu, H. Jiang, F. Han, X. Shi, J. Wu, L. Wang, T. Chen, J. Wang, Y. Zhang, H. Yang, G. Zhang, X. Sun, B. Wang, P. Chen, Y. Wang, Y. Xia, H. Peng, *Nature* **2021**, *597*, 57–63.
[3] X. Fan, X. Ji, L. Chen, J. Chen, T. Deng, F. Han, J. Yue, N. Piao, R. Wang, X. Zhou, X. Xiao, L. Chen, C. Wang, *Nat. Energy* **2019**, *4*, 882–890.
[4] G. Wang, M. Yu, X. Feng, *Chem. Soc. Rev.* **2021**, *50*, 2388–2443.
[5] L. Wang, A. Menakath, F. Han, Y. Wang, P. Y. Zavalij, K. J. Gaskell, O. Borodin, D. Iuga, S. P. Brown, C. Wang, K. Xu, B. W. Eichhorn, *Nat. Chem.* **2019**, *11*, 789–796.
[6] L. Ye, M. Liao, X. Cheng, X. Zhou, Y. Zhao, Y. Yang, C. Tang, H. Sun, Y. Gao, B. Wang, H. Peng, *Angew. Chem. Int. Ed.* **2021**, *60*, 17419–17425.
[7] L. Chen, X. Fan, X. Ji, J. Chen, S. Hou, C. Wang, *Joule* **2019**, *3*, 732–744.
[8] L. Suo, W. Xue, M. Gobet, S. G. Greenbaum, C. Wang, Y. Chen, W. Yang, Y. Li, J. Li, *Proc. Natl. Acad. Sci. USA* **2018**, *115*, 1156–1161.
[9] Z. Chang, Y. Qiao, H. Yang, H. Deng, X. Zhu, P. He, H. Zhou, *Energy Environ. Sci.* **2020**, *13*, 4122–4131.
[10] L. Ye, M. Liao, H. Sun, Y. Yang, C. Tang, Y. Zhao, L. Wang, Y. Xu, L. Zhang, B. Wang, F. Xu, X. Sun, Y. Zhang, H. Dai, P. G. Bruce, H. Peng, *Angew. Chem. Int. Ed.* **2019**, *58*, 2437–2442.
[11] R. Zhang, X. R. Chen, X. Chen, X. B. Cheng, X. Q. Zhang, C. Yan, Q. Zhang, *Angew. Chem. Int. Ed.* **2017**, *56*, 7764–7768.
[12] C. Fang, J. Li, M. Zhang, Y. Zhang, F. Yang, J. Z. Lee, M. H. Lee, J. Alvarado, M. A. Schroeder, Y. Yang, B. Lu, N. Williams, M. Ceja, L. Yang, M. Cai, J. Gu, K. Xu, X. Wang, Y. S. Meng, *Nature* **2019**, *572*, 511–515.
[13] H. Sun, G. Zhu, Y. Zhu, M. C. Lin, H. Chen, Y. Y. Li, W. H. Hung, B. Zhou, X. Wang, Y. Bai, M. Gu, C. L. Huang, H. C.

Tai, X. Xu, M. Angell, J. J. Shyue, H. Dai, *Adv. Mater.* **2020**, *32*, 2001741.
[14] J. Qian, B. D. Adams, J. Zheng, W. Xu, W. A. Henderson, J. Wang, M. E. Bowden, S. Xu, J. Hu, J.-G. Zhang, *Adv. Funct. Mater.* **2016**, *26*, 7094–7102.
[15] Y. Qiao, H. Yang, Z. Chang, H. Deng, X. Li, H. Zhou, *Nat. Energy* **2021**, *6*, 653–662.
[16] L. Lin, K. Qin, Q. Zhang, L. Gu, L. Suo, Y. Hu, H. Li, X. Huang, L. Chen, *Angew. Chem. Int. Ed.* **2021**, *60*, 8289–8296.
[17] C. J. Huang, B. Thirumalraj, H. C. Tao, K. N. Shitaw, H. Sutiono, T. T. Hagos, T. T. Beyene, L. M. Kuo, C. C. Wang, S. H. Wu, W. N. Su, B. J. Hwang, *Nat. Commun.* **2021**, *12*, 1452.
[18] S. Nanda, A. Gupta, A. Manthiram, *Adv. Energy Mater.* **2021**, *11*, 2000804.
[19] A. J. Louli, A. Eldesoky, R. Weber, M. Genovese, M. Coon, J. deGooyer, Z. Deng, R. T. White, J. Lee, T. Rodgers, R. Petibon, S. Hy, S. J. H. Cheng, J. R. Dahn, *Nat. Energy* **2020**, *5*, 693–702.
[20] Z. Yu, P. E. Rudnicki, Z. Zhang, Z. Huang, H. Celik, S. T. Oyakhire, Y. Chen, X. Kong, S. C. Kim, X. Xiao, H. Wang, Y. Zheng, G. A. Kamat, M. S. Kim, S. F. Bent, J. Qin, Y. Cui, Z. Bao, *Nat. Energy* **2022**, *7*, 94–106.
[21] R. Rodriguez, K. E. Loeffler, R. A. Edison, R. M. Stephens, A. Dolocan, A. Heller, C. B. Mullins, *ACS Appl. Energy Mater.* **2018**, *1*, 5830–5835.
[22] Z. L. Brown, S. Heiskanen, B. L. Lucht, *J. Electrochem. Soc.* **2019**, *166*, A2523.
[23] L. Lin, L. Suo, Y. Hu, H. Li, X. Huang, L. Chen, *Adv. Energy Mater.* **2021**, *11*, 2003709.
[24] A. A. Assegie, C. C. Chung, M. C. Tsai, W. N. Su, C. W. Chen, B. J. Hwang, *Nanoscale* **2019**, *11*, 2710–2720.
[25] Z. Li, X. Huang, L. Kong, N. Qin, Z. Wang, L. Yin, Y. Li, Q. Gan, K. Liao, S. Gu, T. Zhang, H. Huang, L. Wang, G. Luo, X. Cheng, Z. Lu, *Energy Storage Mater.* **2022**, *45*, 40–47.
[26] A. J. Louli, M. Genovese, R. Weber, S. G. Hames, E. R. Logan, J. R. Dahn, *J. Electrochem. Soc.* **2019**, *166*, A523.
[27] T. T. Beyene, B. A. Jote, Z. T. Wondimkun, B. W. Olbassa, C. J. Huang, B. Thirumalraj, C. H. Wang, W. N. Su, H. Dai, B. J. Hwang, *ACS Appl. Mater. Interfaces* **2019**, *11*, 31962–31971.
[28] O. Tamwattana, H. Park, J. Kim, I. Hwang, G. Yoon, T.-h. Hwang, Y.-S. Kang, J. Park, N. Meethong, K. Kang, *ACS Energy Lett.* **2021**, *6*, 4416–4425.
[29] Z. Tu, S. Choudhury, M. J. Zachman, S. Wei, K. Zhang, L. F. Kourkoutis, L. A. Archer, *Joule* **2017**, *1*, 394–406.
[30] Y. Gao, Z. Yan, J. L. Gray, X. He, D. Wang, T. Chen, Q. Huang, Y. C. Li, H. Wang, S. H. Kim, T. E. Mallouk, D. Wang, *Nat. Mater.* **2019**, *18*, 384–389.
[31] A. Hu, W. Chen, X. Du, Y. Hu, T. Lei, H. Wang, L. Xue, Y. Li, H. Sun, Y. Yan, J. Long, C. Shu, J. Zhu, B. Li, X. Wang, J. Xiong, *Energy Environ. Sci.* **2021**, *14*, 4115–4124.
[32] W. Chen, R. V. Salvatierra, M. Ren, J. Chen, M. G. Stanford, J. M. Tour, *Adv. Mater.* **2020**, *32*, 2002850.
[33] S. Li, F. Lorandi, H. Wang, T. Liu, J. F. Whitacre, K. Matyjaszewski, *Prog. Polym. Sci.* **2021**, *122*, 101453.
[34] S. Liu, X. Ji, J. Yue, S. Hou, P. Wang, C. Cui, J. Chen, B. Shao, J. Li, F. Han, J. Tu, C. Wang, *J. Am. Chem. Soc.* **2020**, *142*, 2438–2447.
[35] H. J. S. Sand, *Philos. Mag.* **1901**, *1*, 45–79.
[36] T. Li, X. Q. Zhang, N. Yao, Y. X. Yao, L. P. Hou, X. Chen, M. Y. Zhou, J. Q. Huang, Q. Zhang, *Angew. Chem. Int. Ed.* **2021**, *60*, 22683–22687.
[37] R. G. Fedorov, S. Maletti, C. Heubner, A. Michaelis, Y. Ein-Eli, *Adv. Energy Mater.* **2021**, *11*, 2101173.
[38] J. Li, Y. Zhu, W. Chen, Z. Lu, J. Xu, A. Pei, Y. Peng, X. Zheng, Z. Zhang, S. Chu, Y. Cui, *Joule* **2019**, *3*, 557–569.
[39] R. Xu, J. F. Ding, X. X. Ma, C. Yan, Y. X. Yao, J. Q. Huang, *Adv. Mater.* **2021**, *33*, 2105962.
[40] X. B. Cheng, M. Q. Zhao, C. Chen, A. Pentecost, K. Maleski, T. Mathis, X. Q. Zhang, Q. Zhang, J. Jiang, Y. Gogotsi, *Nat. Commun.* **2017**, *8*, 336.
[41] H. Zheng, H. Xiang, F. Jiang, Y. Liu, Y. Sun, X. Liang, Y. Feng, Y. Yu, *Adv. Energy Mater.* **2020**, *10*, 2001440.
[42] J. Holoubek, M. Yu, S. Yu, M. Li, Z. Wu, D. Xia, P. Bhaladhare, M. S. Gonzalez, T. A. Pascal, P. Liu, Z. Chen, *ACS Energy Lett.* **2020**, *5*, 1438–1447.
[43] S. J. Tan, J. Yue, X. C. Hu, Z. Z. Shen, W. P. Wang, J. Y. Li, T. T. Zuo, H. Duan, Y. Xiao, Y. X. Yin, R. Wen, Y. G. Guo, *Angew. Chem. Int. Ed.* **2019**, *58*, 7802–7807.
[44] S. Li, J. Huang, Y. Cui, S. Liu, Z. Chen, W. Huang, C. Li, R. Liu, R. Fu, D. Wu, *Nat. Nanotechnol.* **2022**, *17*, 613–621.
[45] C. Yan, Y.-X. Yao, X. Chen, X.-B. Cheng, X.-Q. Zhang, J.-Q. Huang, Q. Zhang, *Angew. Chem. Int. Ed.* **2018**, *57*, 14055–14059.
[46] X. Fan, L. Chen, O. Borodin, X. Ji, J. Chen, S. Hou, T. Deng, J. Zheng, C. Yang, S. C. Liou, K. Amine, K. Xu, C. Wang, *Nat. Nanotechnol.* **2018**, *13*, 715–722.
[47] C. Heubner, S. Maletti, O. Lohrberg, T. Lein, T. Liebmann, A. Nickol, M. Schneider, A. Michaelis, *Batteries Supercaps* **2021**, *4*, 1310–1322.
[48] Z. Chen, Y. Yan, S. Xin, W. Li, J. Qu, Y.-G. Guo, W.-G. Song, *J. Mater. Chem. A* **2013**, *1*, 11404–11409.
[49] H. Kwon, J. H. Lee, Y. Roh, J. Baek, D. J. Shin, J. K. Yoon, H. J. Ha, J. Y. Kim, H. T. Kim, *Nat. Commun.* **2021**, *12*, 5537.
[50] G. Li, Z. Liu, Q. Huang, Y. Gao, M. Regula, D. Wang, L.-Q. Chen, D. Wang, *Nat. Energy* **2018**, *3*, 1076–1083.
[51] H. Sun, G. Zhu, X. Xu, M. Liao, Y. Y. Li, M. Angell, M. Gu, Y. Zhu, W. H. Hung, J. Li, Y. Kuang, Y. Meng, M. C. Lin, H. Peng, H. Dai, *Nat. Commun.* **2019**, *10*, 3302.
[52] T. Li, X.-Q. Zhang, P. Shi, Q. Zhang, *Joule* **2019**, *3*, 2647–2661.
[53] A. Wang, S. Kadam, H. Li, S. Shi, Y. Qi, *npj Comput. Mater.* **2018**, *4*, 15.
[54] C. Cui, C. Yang, N. Eidson, J. Chen, F. Han, L. Chen, C. Luo, P. F. Wang, X. Fan, C. Wang, *Adv. Mater.* **2020**, *32*, 1906427.
[55] C. Heubner, M. Schneider, A. Michaelis, *Adv. Energy Mater.* **2020**, *10*, 1902523.
[56] R. Saroha, A. K. Panwar, Y. Sharma, P. K. Tyagi, S. Ghosh, *Appl. Surf. Sci.* **2017**, *394*, 25–36.
[57] Z. Yu, D. G. Mackanic, W. Michaels, M. Lee, A. Pei, D. Feng, Q. Zhang, Y. Tsao, C. V. Amanchukwu, X. Yan, H. Wang, S. Chen, K. Liu, J. Kang, J. Qin, Y. Cui, Z. Bao, *Joule* **2019**, *3*, 2761–2776.
[58] C. Heubner, K. Voigt, P. Marcinkowski, S. Reuber, K. Nikolowski, M. Schneider, M. Partsch, A. Michaelis, *Adv. Energy Mater.* **2021**, *11*, 2102647.
[59] Y. Wang, S. Luo, M. Chen, L. Wu, *Adv. Funct. Mater.* **2020**, *30*, 2000373.
[60] C. Heubner, S. Maletti, H. Auer, J. Hüttl, K. Voigt, O. Lohrberg, K. Nikolowski, M. Partsch, A. Michaelis, *Adv. Funct. Mater.* **2021**, *31*, 2106608.
[61] K. Wen, C. Xin, S. Guan, X. Wu, S. He, C. Xue, S. Liu, Y. Shen, L. Li, C. Nan, *Adv. Mater.* **2022**, *34*, 2202143.

Manuscript received: April 8, 2023
Accepted manuscript online: May 4, 2023
Version of record online: May 19, 2023